RESEARCH ARTICLE | JUNE 01 2023

Quantum state-resolved methane scattering from Ni(111) and NiO(111) by bolometer infrared laser tagging: The effect of surface oxidation

Christopher S. Reilly ✉ iD ; Patrick Floß iD ; Bo-Jung Chen; Daniel J. Auerbach iD ; Rainer D. Beck iD

Check for updates

View Online   Export Citation   CrossMark

The Journal of Chemical Physics

Special Topic: Adhesion and Friction

Submit Today!

AIP Publishing

AIP Publishing

Quantum state-resolved methane scattering from Ni(111) and NiO(111) by bolometer infrared laser tagging: The effect of surface oxidation

View Online   Export Citation   CrossMark

Christopher S. Reilly,[1,a)] (ID) Patrick Floß,[1,2] (ID) Bo-Jung Chen,[1] Daniel J. Auerbach,[1,3] (ID) and Rainer D. Beck[1,b)] (ID)

AFFILIATIONS

[1] Institute of Chemical Sciences and Engineering (ISIC), École Polytechnique Fédérale de Lausanne (EPFL), 1015 Lausanne, Switzerland
[2] Max Planck-EPFL Center for Molecular Nanoscience and Technology, Göttingen, Germany
[3] Max Planck Insitute for Multidisciplinary Sciences, Göttingen, Germany

a) Author to whom correspondence should be addressed: christopher.reilly@epfl.ch
b) Electronic mail: rainer.beck@epfl.ch

ABSTRACT

We describe a novel ultrahigh vacuum state-to-state molecule/surface scattering apparatus with quantum state preparation of the incident molecular beam and angle-resolved quantum state detection of the scattered molecules. State-resolved detection is accomplished using a tunable mid-infrared laser source combined with a cryogenic bolometer detector and is applicable to any molecule with an infrared-active vibrational transition. Results on rotationally inelastic scattering of CH_4 methane from a Ni(111) surface and NiO(111)/Ni(111) oxide film, obtained by the new apparatus, are presented. Molecules scattering from the oxidized surface, compared to those scattering from the bare nickel surface, are more highly excited rotationally and scatter into a broader distribution of angles. The internal alignment of molecular rotation is in addition found to be stronger in molecules scattering from the bare surface. Furthermore, the maxima of the state-resolved angular distributions shift toward and away from surface normal with increasing rotational quantum number J for the oxidized and bare surface, respectively. Finally, the rotational state populations produced in scattering from the oxidized surface are well-described by a Boltzmann distribution, while those produced in scattering from the bare surface exhibit large deviations from their best-fit Boltzmann distributions. These results point toward a marked enhancement in molecule–surface collisional energy exchange induced by oxidation of the nickel surface.

I. INTRODUCTION

Detailed information about molecule/surface interactions and energy transfer can be obtained through "state-to-state" molecule/surface scattering experiments, which resolve the quantum state distribution of molecules scattering from a well-defined initial quantum state. State-to-state scattering data are often used for comparison with the predictions of theoretical models based on classical or quantum dynamical description of the molecule/surface interactions with the aim of developing predictive models of heterogeneous catalysis.[1,2] Because the scattered species are usually dispersed by scattering angle, recoil velocity, and quantum state, a sensitive

state-specific detection method is required in order to obtain high-quality experimental data.

Laser induced fluorescence (LIF)[3] and resonant enhanced multiphoton ionization (REMPI)[4] are two widely used detection techniques for state-to-state scattering experiments. While LIF and REMPI deliver high detection sensitivity, their application is limited to molecules that possess excited electronic states with lifetimes long enough to permit resolution of individual rotational transitions.

IR absorption is a more broadly applicable state-specific detection technique. It has the advantage over LIF and REMPI of being applicable to any molecule with an infrared-active vibrational mode and a rotationally resolved gas phase spectrum. Sensitive detection of

IR absorption can be accomplished using optothermal spectroscopy[5] where the molecules excited by the IR radiation impinge on a sensitive cryogenic bolometer detector and the absorption is detected indirectly by the extra heat input transferred to the bolometer from the excited molecules. Applied to state-resolved scattering experiments, this technique uses a tunable, single mode, continuous-wave (CW) IR laser to excite or "tag" scattered molecules in a specific quantum state as they fly toward a cryogenic bolometer. We refer to this method as the BILT detection technique, standing for bolometric infrared laser tagging.

Many important molecules, like methane and carbon dioxide, that have no demonstrated LIF or REMPI detection scheme can be readily detected using BILT. Another advantage of BILT over LIF and REMPI is the ease of converting measured BILT signals to state population distributions. Both LIF and REMPI yield signals that are proportional to sample density and therefore require a density to flux conversion in addition to a state-specific calibration procedure to extract state populations from the spectral intensity. The signals produced by BILT on the other hand are directly proportional to the flux and therefore provide a direct measure of relative state populations.

The basic principle of BILT detection was originally developed by the group of R.E. Miller, who used color center lasers in combination with a multi-pass cell for infrared excitation of surface scattered methane and acetylene from a LiF surface in high vacuum.[6–9] Technological advances in the years following these initial studies have made possible important improvements on the BILT technique. First, with the high power (>1 W) and narrow-bandwidth (<1 MHz) tunable CW mid-infrared optical parametric oscillator (OPO)-based lasers now commercially available,[10,11] it is possible to saturate C–H and C–O stretch vibrational transitions in a single pass of the laser through the scattering plane, obviating the need for complicated *in situ* multi-pass optics. In addition, improvements in bolometer construction now permit operation in ultrahigh vacuum (UHV), extending the applicability of the BILT technique to scattering from more reactive surfaces, including metal catalysts.

We have recently[12,13] reported results using BILT detection for state-to-state molecule/surface scattering from both a clean single crystal metal surface and a graphene overlayer in ultrahigh vacuum (UHV). The experiment was based on a UHV apparatus designed for molecular beam/surface reactivity measurements that was modified to include a bolometer attached to a side port. Even though the bolometer used was not fully UHV compatible and the vacuum in the scattering chamber was somewhat degraded, by maintaining the surface at 400 °C, we were able to measure vibrational and rotationally inelastic scattering from both the bare Ni(111) surface and graphene overlayer. The results show there is a facile collision-mediated conversion of antisymmetric (v_3) CH$_4$ stretching motion to symmetric (v_1) stretching motion for scattering from Ni(111), which is absent in scattering from graphene. The facile $v_3 \rightarrow v_1$ conversion reflects an influence exerted by the reactive Ni(111) surface on the C–H bond that may relate to the surface's ability to catalyze dissociative chemisorption. The absence of $v_3 \rightarrow v_1$ conversion on the presumably much less reactive graphene overlayer lends further support to the notion of measurable correlations between scattering behavior and chemical reactivity.

More importantly and more generally, scattering measurements offer a perspective on the molecule/surface interaction that is complementary to the perspective provided by measurements of state-specific reactivity measurements, of which for the CH$_4$/Ni(111) system there are many.[14–20] Although these studies provide detailed information on the microscopic reaction mechanism of methane dissociation on Ni(111), the measurements probe only the portion of molecules that react and ignore the scattered molecules, which often account for the vast majority of the incident flux (the reaction probability for methane on nickel at surface temperatures below 400 K is for example only ~10^{-6}). Furthermore, the reactive and nonreactive trajectories will explore different regions of the potential energy surface, with the region explored by the non-reactive trajectories being the larger to the extent that the reaction is rare. In any case, combining the information on the reactive and nonreactive channels provides a more comprehensive test of theory than either dataset alone.

An additional benefit of scattering measurements concerns the relative quality of the available probes. Any dynamical information on the reactive trajectories that are imprinted transiently on the rovibrational state of the reacted species is inaccessible to available probes of surface-bound species, either because of the limitations of the selected probe or because of rapid quenching of internal excitations by the surface degrees of freedom. Rovibrational excitations of the scattered species returning to the gas phase are however sufficiently long-lived that they can easily be resolved using well-established techniques of high-resolution gas phase spectroscopy, including the optothermal technique we employ in our BILT system. So, while reactivity measurements are typically limited to testing a single observable of a dynamical theory, namely, the reaction probability, state-resolved scattering measurements can offer a much more stringent test since a successful theory must reproduce not just a single observable but the full rovibrational state distribution of the scattered flux.

Although the $v_3 \rightarrow v_1$ scattering experiments discussed above clearly demonstrated the applicability of BILT to scattering from reactive metal catalysts, the experimental setup had significant limitations. First, the sum of the incident and scattered angle for this apparatus was fixed at 135°, making it impossible to study independently the scattering as a function of incidence and final angles. Additionally, the distance from the surface to the bolometer was large, limiting the sensitivity. Last but not least, the bolometer used was not fully UHV compatible, limiting the range of surface compositions and surface temperatures that could be studied.

In this paper, we describe the design and implementation of a new molecular beam/surface scattering instrument that overcomes these limitations. The new instrument includes a rotatable cryogenic bolometer allowing independent variation of the incident and scattering angles. It uses a custom-designed UHV bolometer with a geometry optimized to probe a wide range of scattering angles, along with two independently tunable OPO systems for state preparation of the incident molecules and BILT detection of the scattered molecules. Extensive use of computer control of the laser systems, bolometer detection angle, and positioning of the tagging laser beam enables us to obtain angle-resolved state-to-state scattering information for a broad range of molecules comparable to that available for molecules with sensitive REMPI or LIF detection schemes.

We demonstrate the capabilities of the new instrument by applying the BILT technique to the study of rotational inelasticity in CH_4 scattering from both the bare and oxidized Ni(111) surface. To avoid any potential for confusion in later sections of the paper, we emphasize now that, while in the apparatus description (Sec. II) we describe for the sake of future reference a laser-based capability for preparation of molecules excited vibrational states, the main results presented in Sec. III pertain to molecules scattering from the ground vibrational state without any initial laser excitation. The surfaces studied were selected in order to investigate how the chemical modification of a catalytic surface changes the surface's physical influence on scattering molecules. Evidence of rotational excitation in scattering of methane molecules in their ground vibrational state from the Ni(111) surface was already available from a previous non-state-resolved scattering experiment. Sharp peaks in the angular distributions of scattered molecules measured in the study were attributed to coherent diffraction of molecules excited rotationally by the surface collision.[21]

A well-characterized oxide film is readily grown on Ni(111) by exposure to O_2. Oxidation of Ni(111) at low temperatures (<400 K) produces a self-terminating thin film of NiO, 2–3 monolayers in thickness, that exposes the (111) facet of the NiO crystal.[22–26] Low energy electron diffraction (LEED) measurements and electron microscopy measurements[26] indicate that the oxide film is broken up into small domains roughly 1.3 nm in size. The NiO(111) facet is peculiar in that it yields a bulk-terminated "polar" surface that is energetically unstable due to electrostatic interactions between the charged planes of alternating polarity.[27] These films are thought to be stabilized by adsorption of charged hydroxyl species originating from water present in the UHV background. This hypothesis is supported by inelastic electron scattering measurements observing spectral features consistent with excitation of O–H stretches on the oxide surface.[24]

Helium atom scattering (HAS) measurements provide a perspective on the nature of the lateral corrugation in the interaction potentials presented by the nickel and nickel oxide surfaces to scattering atoms/molecules. HAS measurements[28] on the single crystal NiO(100) for example exhibit strong diffraction peaks consistent with a sizable lateral corrugation in the atom-surface potential (characteristic depth 0.14 Å), while similar measurements on Ni(111)[29,30] imply a corrugation depth of only 0.007(2) Å. Our own HAS measurements performed on the Ni(111) surface and NiO(111)/Ni(111) oxide film (see Sec. S2 of the supplementary material) also indicate a marked increase in surface corrugation upon oxidation.[31]

The state- and angle-resolved scattering data obtained from our new instrument allow us to analyze trends in both angular and rotational state distributions as well as correlations between these trends. Compared to the unoxidized Ni(111) surface, molecules scattering from the oxidized surface are more excited rotationally and possess a broader angular distribution peaking closer to surface normal. In addition, the peak angles of the quantum state-resolved scattering distributions show a strong negative correlation with the state's angular momentum quantum number J for scattering from the oxidized Ni(111) surface, while for the bare surface the correlation is strongly positive. The degree of rotational excitation in scattering from the oxidized surface is further found to be sensitive to changes in surface temperature, while for the bare surface rotational excitation shows only a minor temperature effect. By combining the analysis across the different experimental dimensions accessible to our state-to-state BILT technique, we arrive at a robust conclusion of a dramatic increase in collision-mediated molecule–surface energy exchange upon surface oxidation, affirming the notion that chemical modification of a surface should produce clear physical effects in the molecule scattering behavior.

II. DESCRIPTION OF APPARATUS

To motivate the detailed descriptions to come in the following subsections, we first present in Fig. 1 a diagram illustrating schematically a prototypical state-to-state scattering experiment "tailor-made" for our newly constructed apparatus. In this prototype experiment, a molecular beam with a narrow velocity distribution is directed at a clean single crystal surface scattering target located in an ultrahigh vacuum (UHV) chamber. Before striking the surface, a significant fraction of the incident molecules are prepared into a specific rovibrational quantum state by an infrared pump laser beam. Scattered molecules are detected with quantum state resolution using a second tunable infrared laser that "tags" the molecules by adding vibrational energy selectively to molecules that have scattered into a particular rovibrational quantum state. Tagged molecules are detected selectively by lock-in techniques when they transfer the energy gained in the tagging excitation to a cold (1.8 K) silicon bolometer detector. By measuring the energy absorbed by the bolometer as the tagging laser is tuned to different rovibrational transitions, the rovibrational state distribution of the scattered molecules is reconstructed, and by rotating the detector and tagging
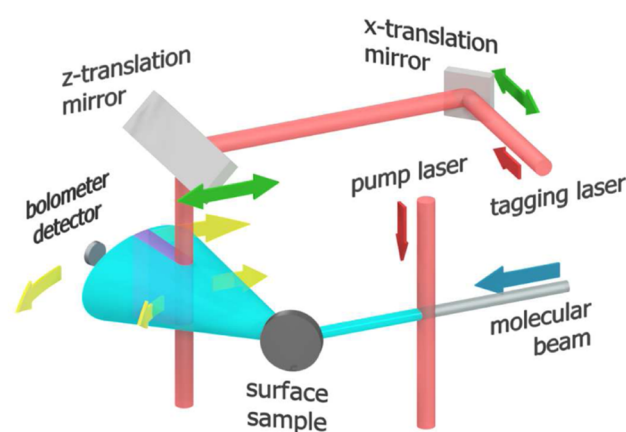
FIG. 1. Schematic diagram of the state-to-state experimental technique described in this work. A molecular beam from a supersonic expansion is pumped by the IR pump laser to a specific incident rovibrational state. The molecules scatter from the surface of a sample at a controlled incidence angle. Scattered molecules at a specific scattering angle transfer energy resonantly absorbed from a IR tagging laser to a 1.8 K Si bolometer detector. The blue arrow denotes the direction of the incident molecular beam. The red arrows denote the directions of propagation of the pump and tagging laser beams. The tagging laser beam and bolometer can be rotated about an axis that is perpendicular to the scattering plane and intersects the point of intersection of the molecular beam and the surface. The positioning of the tagging laser beam is accomplished using two mirrors mounted on translation stages with perpendicular directions of translation. Each green arrow denotes the direction of translation of its associated tagging mirror. The yellow arrows denote the synchronized rotation of the detector and tagging laser.

laser about the surface we obtain rotational state distributions over a range of scattering angles.

The apparatus we have designed and constructed to carry out the types of experiments just described contains a number of interconnected subsystems, including a molecular beam source, a sample holder/manipulator with sample heating and cooling capabilities, a pump laser for initial state preparation, a tagging laser for final state detection, and a rotatable cryogenically cooled bolometer detector. In the remainder of this section, we give a detailed description of these subsystems as they are implemented in our recently constructed apparatus.

A. Scattering apparatus

A 2-D cross section through the scattering plane of the state-to-state molecular beam surface scattering instrument is shown in Sec. II. The vacuum system has four stages of pumping: the source chamber with a 2000 L s^{-1} turbo pump (STP-iXR2206, Edwards); a first differential pumping stage with a 500 L s^{-1} turbo pump (TMU520, Pfeiffer); a second differential pumping stage with a 510 L s^{-1} turbo pump (TMU521, Pfeiffer); and finally the UHV scattering chamber with a 880 L s^{-1} turbo pump (TMU1000, Pfeiffer). The blades of the UHV chamber turbo pump are protected from potentially falling debris by a mesh screen that reduces the pump's effective speed to 625 L s^{-1}.

The source chamber ($P1$ in Fig. 2) contains a custom temperature controlled expansion nozzle used to generate the molecular beam. The nozzle consists of a 6 mm diameter metal tube held by water-cooled copper clamps that serve to pass electrical current through the thin walled tube for nozzle heating. A 60 μm laser-drilled hole is located at the center of the 100 mm long nozzle tube through which gas expands from a stagnation pressure of 2–3 bars into the 10^{-4} mbar vacuum of the source chamber. The nozzle is mounted on an x-y-z manipulator that allows alignment of the nozzle opening with a 1 mm diameter aperture skimmer (Model 2, Beam Dynamics) separating the source chamber and first differential pumping stage.

The first differential pumping stage ($P2$) houses a molecular beam chopper consisting of a brushless DC motor (Maxon EC 32) with integrated encoder that spins a 127 mm diameter copper-beryllium chopper disk with two diametrically opposed 2 mm slits at speeds up to 200 Hz. An optocoupler straddling the chopper disk allows for synchronization of data acquisition devices to the chopped molecular beam. Synchronization is required for time-of-flight measurements of the molecular beam velocity distribution using a quadrupole mass spectrometer with a cross beam ionizer (Pfeiffer QMG 220) as well as synchronous detection of the energy flux arriving on the bolometer detector from the chopped molecular beam (see Sec. II B). Optical access to the molecular beam is available in the first differential pumping stage through antireflection (AR) coated CaF$_2$ windows. Infrared radiation from a tunable, continuous-wave infrared optical parametric oscillator (Aculite Argos) is used for state-specific preparation of the incident molecular beam (see Sec. II C 2).

The second differential pumping stage ($P3$) contains a retractable pyroelectric detector (Eltec, 406M70-o) that serves to quantify the efficiency of state preparation.[32] A homebuilt manual separation valve between the first and second differential pumping
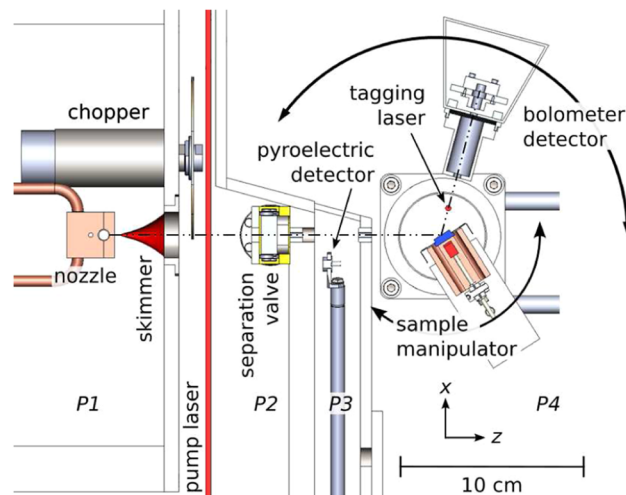
FIG. 2. Simplified cross-sectional view of the xz-scattering plane showing the spatial layout of the main components of the molecule/surface scattering instrument. The red box inside the sample manipulator represents the tungsten filament used for radiative and electron-beam heating of the surface sample, represented by the stepped blue disk. $P1$ designates the source chamber and $P4$ designates the UHV/scattering chamber, while $P2$ and $P3$ designate the two stages of differential pumping isolating $P4$ from $P1$. See text body for complete description of components.

stages permits venting of the source chamber and the first differential pumping stage without breaking UHV conditions in the scattering chamber.

The UHV scattering chamber ($P4$, base pressure 1 × 10^{-10} mbar) houses the surface sample and the rotatable bolometric detector in addition to several instruments for surface cleaning and analysis (see below). A Teflon beam flag mounted on a UHV-compatible stepper motor can be used to block/unblock the molecular beam at the entrance of the UHV scattering chamber. This ability permits measurement of sticking coefficients by the beam reflectivity (King & Wells) method.[33]

Surface samples (i.e., scattering targets) are mounted on a tantalum support, which is electrically insulated from but in good thermal contact with a liquid nitrogen-cooled copper support housing a tungsten filament for electron-bombardment and radiative sample heating. A four-axis manipulator allows for accurate sample positioning along the xyz-axes and for sample rotation about an axis perpendicular to the xz plane. For scattering experiments, the sample is positioned so that the incident molecular beam strikes the center of the sample and its rotation axis coincides with the axis of rotation of the rotatable lid holding the bolometer detector (Sec. II B). A 1.75 mm diameter aperture collimates the molecular beam entering the chamber and constrains the beam to intersect the rotating lid's rotation axis. The molecular beam's diameter (≈100% flux) at the surface is 2.3 mm as calculated from the diameters and locations of the nozzle and limiting aperture. The skimmer to surface distance is 175 mm and the surface to bolometer distance is 85 mm.

The 4 mm diameter tagging laser beam used for state-specific excitation of the scattered molecules enters the UHV chamber from above (i.e., along the y-direction from Sec. II) through a

differentially pumped AR-coated CaF_2 window and passes in front of the scattering surface at a distance of 15 mm. Two 50.8 mm diameter Au mirrors mounted on motorized linear translation stages (Physik Instrumente VT-80) with orthogonal directions of translation allow us to position the tagging laser beam so that it is positioned between the surface sample and the bolometer detector as the detector is rotated (see Fig. 1). As depicted in Sec. II, the sample holder is mounted on a tube with a 47 mm clear aperture in order to let the tagging laser beam exit the UHV chamber through a differentially pumped AR-coated CaF_2 window located at the bottom of the UHV chamber.

The scattering chamber is additionally equipped with an Omicron ISE100 ion sputtering gun for removal of surface contaminants. A connected leak valve allows for a controlled exposure of the surface to various gases for oxidative/reductive cleaning or preparation of films/adsorbate overlayers. Chemical composition analysis of the surface is performed by Auger electron spectroscopy (AES) with a cylindrical mirror analyzer system (Staib Instruments, ESA150). The surface structure can be analyzed by low energy electron diffraction (LEED) using a 3-grid LEED optic (OCI Vacuum Microengineering, BDL800). An additional quadrupole mass spectrometer (SRS, RGA 100) is used for residual gas analysis of the UHV background gas composition.

B. Rotatable bolometer detector

See Fig. 3 for a diagram of the bolometer detector assembly and its integration into the rotating platform. The bolometer detector assembly is a customized UHV version of the HDL-5 model from Infrared Laboratories designed for optothermal spectroscopy.[5] The actual bolometer element is a tiny $0.3 \times 0.2 \times 0.1$ mm doped silicon chip whose resistance at cryogenic temperatures responds sensitively and rapidly (500 Hz bandwidth) to changes in heat flow. Bonded to the bolometer element is a 4 mm diameter synthetic diamond absorber element that receives the flux of scattered molecules and transmits the absorbed heat to the bolometer element. A reflective Cr/Au coating is applied to the backside of the diamond absorber to reduce the bolometer's sensitivity to background radiation and scattered laser light. The absorber/bolometer pair is suspended by two small diameter copper wires that are in thermal contact with a support cooled to 1.8 K. A 15 V battery connected in series with a 20 MΩ resistor (not shown) forms a current source, which generates a voltage drop across the bolometer element in proportion to its temperature-dependent resistance. The voltage drop is pre-amplified by an *in vacuo* transistor heated to 60 K and followed by a second ex vacuo amplifier stage (Infrared Laboratories, LN-6C). The second amplifier has been modified to allow for electronic gain selection to facilitate automated data collection. Following amplification, the signal is fed to a lock-in amplifier (SR 830, Stanford Research Systems) for synchronous detection. For quantum state-specific measurements, the lock-in reference oscillator is synchronized to a mechanical chopper, which modulates (f_{mod} = 237 Hz) the intensity of the tagging laser light reaching the scattering chamber. To measure the energy coming from all quantum states populated in the scattered flux, the tagging laser is blocked and the lock-in is referenced to the molecular beam chopper, which modulates the intensity of the incident molecular beam
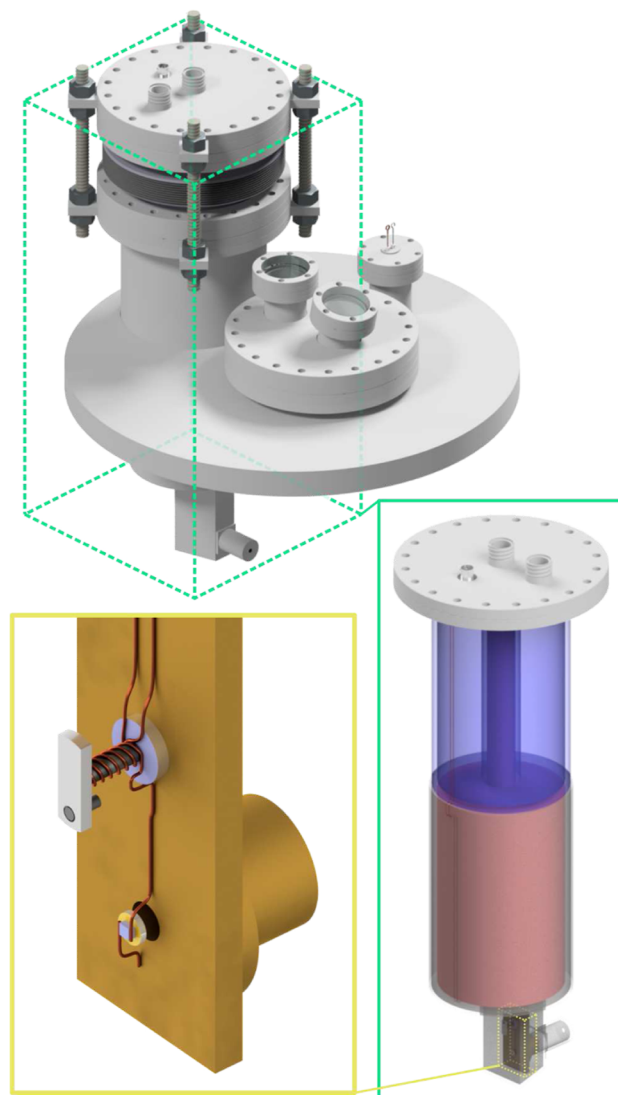
FIG. 3. Schematic illustration of bolometer detector and rotating platform. *Upper left*: rotating platform. Shown are the bolometer detector assembly, tagging laser windows, and thermocouple feedthrough. *Lower right*: bolometer assembly. The blue and red volumes are the liquid nitrogen and liquid helium reservoirs, respectively. *Lower left*: bolometer support. On the lower half is shown the silicon bolometer bonded to the synthetic diamond absorber, and on the upper half is shown the JFET bolometer preamplifier fixed to a thermally insulating standoff. The backside of the bolometer/absorber pair is shown exposed for illustrative purposes. In reality, it is shielded from radiation by a copper enclosure in thermal contact with the liquid helium reservoir.

(f_{mod} = 237 Hz as well). See Fig. 9 for a plot of data obtained using the two techniques.

The bolometer element is mounted on a narrow copper bar attached to the liquid helium reservoir. The compact size of this support structure allows the detector to access a wider range of scattering angles than would be possible if the bolometer element were mounted directly below the liquid helium Dewar. To increase

the hold time of the helium reservoir, the reservoir and support are protected from thermal radiation by an aluminum shield in thermal contact with a liquid nitrogen Dewar above. To improve the bolometer signal-to-noise ratio, the liquid helium reservoir is actively pumped to bring the reservoir temperature below the superfluid transition temperature occurring at 2.17 K. From the vapor pressure measured in the helium reservoir, we estimate a reservoir temperature of 1.8 K during operation. A cylindrical collimator mounted to the cold shield limits the field of view of the bolometer in order to minimize the heat load due to thermal background radiation. Several baffles (not shown) are integrated into the collimator to reduce background noise caused by scattered tagging laser radiation reaching the detector element. At operating temperature, we estimate that one second of signal averaging is sufficient to detect energy fluxes as low as 6.1×10^{-8} W, which, with the tagging laser tuned to excite for example the methane stretch fundamental at 3000 cm^{-1}, corresponds to a state-selected flux of molecules of 5×10^8 molecules/s.

The detector system is mounted on a UHV-compatible rotatory platform. The seal of the rotary platform is based on a design described in the work of Auerbach et al.[34] A software-controllable stepper motor (Trinamic, PD60-4-1160-TMCL) connected to the platform through a reduction gear and a chain drive mechanism (total reduction factor of 175) rotates the platform. The cryogenic bolometer detector assembly is attached to the rotation platform via a flexible bellows supported by four threaded rods allowing fine adjustment of the detector position by turning of nuts screwed on the threaded rods. Optical access occurs via a differentially pumped window flange mounted on the rotary platform housing an AR-coated CaF$_2$ window (differential pumping not shown). A second identical window port is positioned just next to the tagging window in line with the bolometer detector. With the addition of an *in vacuo* mirror just in front of and below the detector, this second window can serve as an exit window for measurement of the velocity distributions of scattered molecules via Doppler velocimetry.[35] In addition, the rotary platform houses a feedthrough for a thermocouple (type-T) used to monitor the temperature of the bolometer cold shield.

C. Infrared laser systems

1. Tagging laser

Quantum state-specific tagging of the scattered molecules is accomplished using the idler output of a tunable, continuous-wave, optical parametric oscillator (TOPO, Toptica Photonics) with >1 W of output power over a range of 2500–4000 cm^{-1}, covering light atom stretch vibration, such as C–H(D), N–H(D), and O–H(D). Figure 4 shows a diagram of the tagging laser system, complete with additional optics and electronics used for frequency measurement and stabilization, linewidth-broadening, and laser power monitoring functions.

A two-stage algorithm, implemented[36] in python, based on Ref. 11 was developed to rapidly (<60 s) tune the idler frequency to within 30 MHz of an arbitrary target frequency within the laser's tuning range. The protocol consists of a coarse-grained tuning stage followed by a fine-grained stage. The coarse-grained stage begins by initialization of the OPO cavity etalon and fan-out PPLN crystal positions to the values associated with the target frequency via
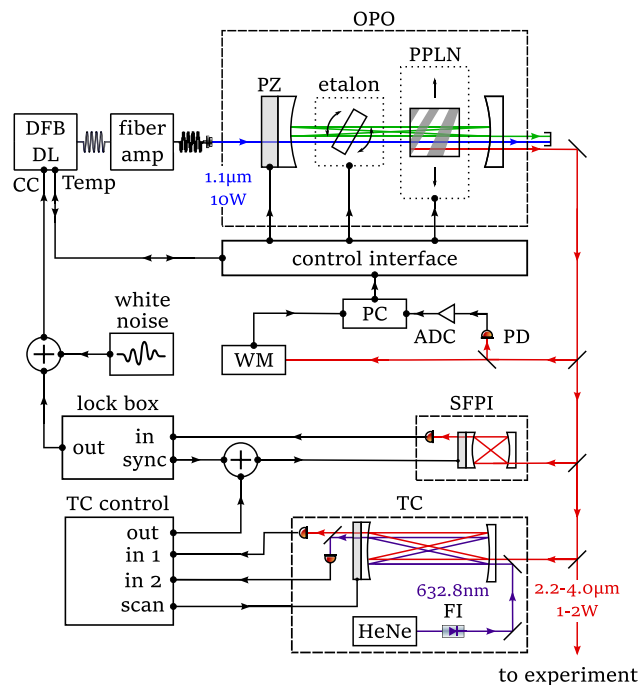
FIG. 4. Diagram of the tagging-OPO stabilization system. **PZ**: piezoelectric strain element; **SFPI**: scanning Fabry–Pérot interferometer; **TC**: transfer cavity; **DFB DL**: distributed feedback diode laser; **CC**: current control; **PPLN**: periodically poled lithium niobate crystal; **WM**: wavemeter; **PD**: photodiode; **ADC**: analog to digital converter; **FI**: Faraday isolator.

a look-up table.[11] The OPO cavity etalon and fan-out PPLN crystal position are then iteratively adjusted while feeding back on the idler output power (via a Thorlabs PDA07P2 photodetector) and wavelength (via a Bristol 671B-MIR wavemeter) in order to bring the measured idler frequency to within 0.5 cm^{-1} of the target with near-optimal output power. For fine-grained tuning, the temperature of the diode laser (DFB pro BFY, Toptica Photonics) seeding the OPO pump is adjusted until the idler frequency matches the target within the 0.001 cm^{-1} (30 MHz) long-term accuracy of the wavemeter. While the seed laser can in principle be temperature-tuned over several cm^{-1}, we have found that reducing the temperature tuning range to 0.5 cm^{-1} helps to limit to an acceptable level the occurrence of mode hops during both temperature tuning and the tagging measurements that follow. We typically encounter only couple mode hop-related interruptions to our measurements over the course of a 10-h session. It is also worth mentioning that for both coarse- and fine-tuning, there are occasions where the measured frequency fails to converge toward the target, presumably due to jumping between different OPO cavity modes. In these cases, we have found that shifting the voltage applied to the OPO cavity piezo by some random amount is sufficient to eliminate the problem. All adjustments of the OPO and seed laser parameters are performed via a digital laser control interface (DLC Pro, Toptica Photonics).

The 30 MHz long-term (1 h) accuracy and 5 MHz short-term (1 s) accuracy of the wavemeter are insufficient to ensure stable and efficient tagging of scattered molecules. Additional frequency
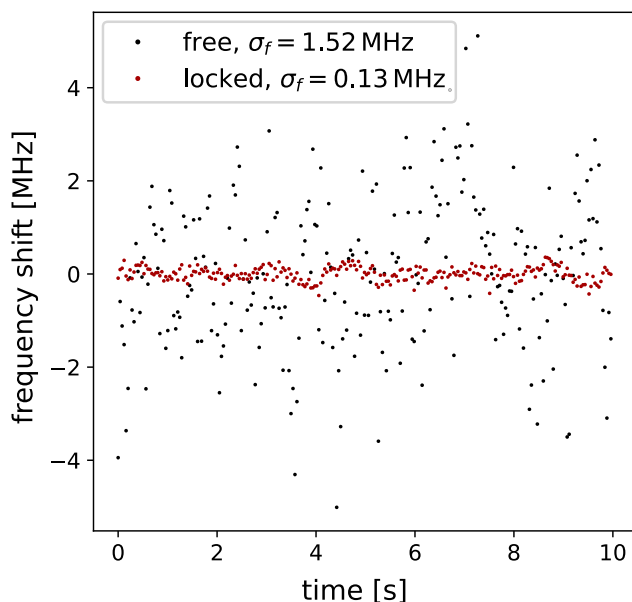
FIG. 5. Performance of short-term frequency stabilization of tagging laser idler by locking to a high finesse Fabry–Pérot optical cavity. Plot shows the fluctuations in idler frequency as measured by the transfer cavity, with (red) and without (black) short-term frequency stabilization. The legend reports the average of the standard deviation computed for ten segments of 1-s duration, roughly equal to the response time of the transfer cavity servo loop. Closed-loop operation gives more than an 11-fold reduction in frequency fluctuations over open-loop operation.

FIG. 6. Demonstration of the response of idler frequency (black points) as measured by the transfer cavity to a 20 MHz shift in the transfer cavity setpoint at $t = 0$. Also plotted is the wavemeter output (red open circles) over the same time interval, to give a comparison of the relative precision of the two frequency measurement devices.

stabilization is therefore necessary to keep the tagging laser resonant with the narrow (20 MHz) linewidth rovibrational transitions for the 30 min duration required to measure a state-resolved angular distribution. For long-term (1 s–1 h) stability, we employ a transfer cavity technique,[37] described below, that requires a level of short-term (1–1000 ms) stability better than that obtained with the laser in free-running operation. To achieve adequate short-term stability, a portion of the idler output is fed to a high finesse, high thermal stability scanning Fabry–Pérot interferometer (FPI, Thorlabs SA200-30C), and a servo loop adjusts the seed laser diode current to lock the idler to the peak of an FPI transmission fringe. See Fig. 5 for a demonstration of the effect of short-term frequency stabilization on transfer cavity performance.

Stability on the second to hour timescale is accomplished using a transfer cavity system employing a homebuilt scanning Fabry–Pérot confocal cavity (250 MHz free spectral range, finesse of 10) in conjunction with a frequency-stabilized helium–neon reference laser (Melles Griot, 05-STP-911) to "transfer" the stability of the reference laser to the idler frequency. The system is in principle the same as that described in Ref. 37, with the polarizing beam splitters replaced by dichroic mirrors and the analog servo loop replaced by a custom software-based procedure. The derived error signal is applied to the piezo controlling the cavity length of the FPI, which in turn controls the idler frequency. The combination of short- and long-term stabilization systems results in an idler output that is stable to within 0.1 MHz on a 1 s time scale and responds to changes in the set point in <1 s (see Fig. 6). To verify that the transfer cavity is able to maintain a constant idler frequency for extended
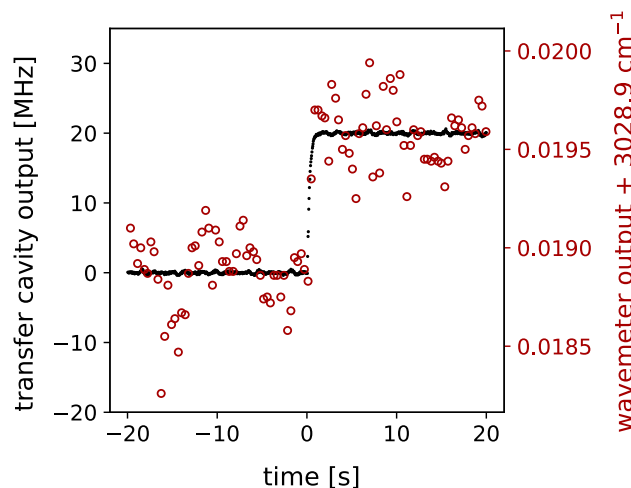
durations, we fed a Lamb-dip stabilized infrared beam[38] to the transfer cavity and monitored the resulting error signal. Over a period of two hours, the frequency of the stabilized laser as measured by the transfer cavity was found to drift by no more than 1 MHz.

One side effect of the high molecular flux design of the scattering apparatus is the broad (3°) angular acceptance of the detector. Since, via the Doppler effect, the frequency of a molecular transition depends on the molecule's velocity in the direction of laser propagation, a wide angular acceptance results in significant Doppler-broadening of the linewidth of a tagging transition. For example, molecules scattering with a velocity of 1000 m/s–the mean velocity of a molecular beam of pure methane generated from a room temperature nozzle–will present to the detector a 15 MHz-wide distribution of transition frequencies for the ν_3 stretch fundamental at 3000 cm^{-1}. Although this linewidth is not large enough to prevent resolution of the rotational spectra of most small molecules, it is large enough to prevent the tagging laser, whose intrinsic linewidth is <2 MHz, from exciting the full distribution of molecules impinging on the detector.

To overcome this problem, we increase the tagging laser linewidth by modulating the diode current of the seed laser with a 60 MHz bandwidth white noise source. A homebuilt 1 MHz cutoff-frequency second-order LC passive high pass filter eliminates frequency fluctuations on timescales slower than the 1 μs transit time of the molecules through the laser beam, since such fluctuations will not improve tagging efficiency.

Figure 7 demonstrates the influence of addition of frequency noise to the tagging laser for different tagging conditions. At high tagging laser intensities, the addition of frequency noise leads to a more than threefold increase in tagging efficiency when the tagging laser is positioned to excite scattered molecules. This can be explained roughly by observing that a single velocity class whose width is equal to twice the Rabi frequency of the transition[39] can be saturated in one-half of a Rabi cycle. If the laser is intense enough
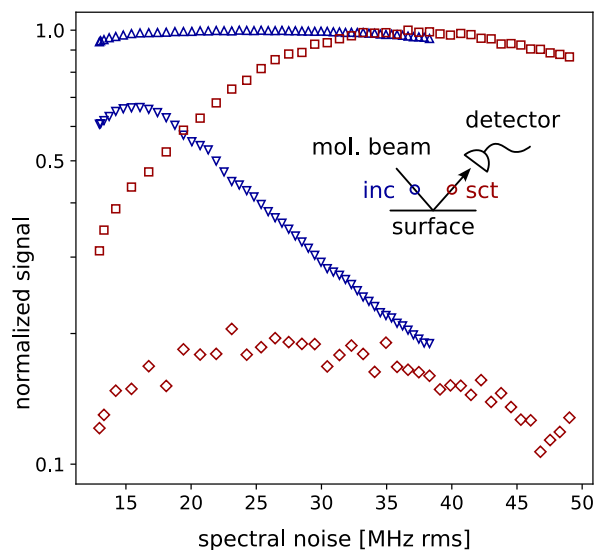
	geometry	intensity (W/cm^2)	Rabi frequency (MHz)	Rabi cycles
△	inc	6.0	2.0	6.0
▽	inc	0.35	0.5	1.5
□	sct	4.7	1.8	3.6
◇	sct	0.51	0.6	1.2

FIG. 7. Effect of spectral line broadening on tagging efficiency. For all measurements, a molecular beam of methane (CH_4) is scattered from a metal surface and the tagging laser is tuned to methane's R(0) ν_3 fundamental transition. The `inc` (blue) and `sct` (red) geometries refer to measurements taken with the tagging laser positioned to excite the incident and scattered molecules, respectively. For the incident and scattered measurements, the molecular beam before scattering has a mean velocity of 1000 and 2900 m s^{-1}, respectively. Data with the same tagging geometry are uniformly scaled to give a maximum response of unity. Laser intensity is computed from measurements of laser power and beam diameter. Rabi frequencies are computed from laser intensity, transition dipole moment,[39] and transition frequency. The number of Rabi cycles is obtained by multiplying the Rabi frequency by the estimated transit time of molecules through the tagging beam.

to drive several Rabi cycles over the course of the molecule transit time through the tagging laser beam, then several velocity classes can be saturated by dithering the laser frequency over a range of several Rabi frequencies, thus improving the overall tagging efficiency. On the other hand, if the tagging laser intensity is so low that the time for one Rabi cycle approaches the molecule transit time, then the tagging efficiency is optimized by targeting a narrow range of frequencies covering only the few most populated velocity classes.

When the tagging laser is positioned to excite the incident molecular beam, we observe little advantage in dithering the frequency. Though this is expected at low laser intensities by the argument just presented, we observe a similar lack of improvement in tagging efficiency even at high laser intensities. This is explained by the low (0.5°) divergence of the molecular beam, which results in a narrow distribution of transition frequencies contained in a single velocity class.
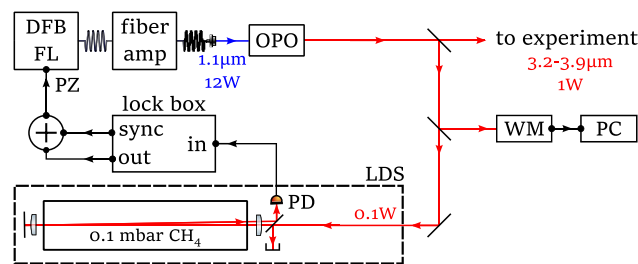
FIG. 8. Diagram of the pump laser frequency stabilization system. **DFB FL**: distributed feedback fiber seed laser; **OPO**: optical parametric oscillator; **PZ**: piezoelectric fiber strain element; **WM**: wavemeter; **LDS**: Lamb-dip system; **PD**: InSb photodiode. For more information on the Lamb-dip frequency stabilization technique, see Ref. 38.

2. Pump laser

Laser excitation serves as a means of rovibrational quantum state preparation of the molecular beam. To generate the laser radiation, we use another mid-IR OPO (Lockheed Martin, Argos Acculight Module C), which provides 1 W of narrow linewidth (50 kHz) output idler power tunable from 2550 to 3150 cm^{-1}.

To stabilize the idler frequency to a molecular transition, a servo loop monitors the transmission of small fraction of the idler output through a Lamb-dip cell and modifies the OPO pump frequency via a piezo element, which strains the seed laser fiber.[38] See Fig. 8 for a diagram of the pump laser frequency stabilization system. Before crossing the molecular beam, the pump laser passes through a cylindrical CaF$_2$ lens (f = 25.4 cm, not shown). The molecules cross a diverging pump laser, producing an effective sweep of the laser frequency that acts to coherently transfer, with nearly 100% efficiency, the molecules from the lower to upper energy state.[32]

D. Demonstration of angle-resolved tagging measurements

To provide a sample of the type of measurements that can be obtained by coordination of the different system components described in this section, we show in Fig. 9(a) collection of state-resolved angular distributions for CH_4 scattering from a Ni(111) surface. Before discussing the plot and the procedure used to obtain the plotted data, we note that the measurements shown probe CH_4 molecules in their ground vibrational state. We therefore do not use the pump laser described in Sec. II C 2 and illustrated in Fig. 1. For investigating scattering dynamics of vibrationally excited molecules, the pump laser can be included without modification of the procedure described below.

Each blue shaded region corresponds to the sum of angle-resolved tagging measurements of the state-selected scattered flux for all sublevels of a given rotational level with total angular momentum quantum number J. Each measurement begins by positioning the bolometer and tagging laser at a detection (scattering) angle where the expected molecular flux is some significant fraction of the peak flux. The tagging laser is then tuned and stabilized to the expected transition frequency of a particular sublevel (see Sec. II C 1). To optimize the tagging efficiency, the laser frequency is scanned until a ~20 MHz-wide resonance in the detector response is resolved, at which point the tagging laser is stabilized to the
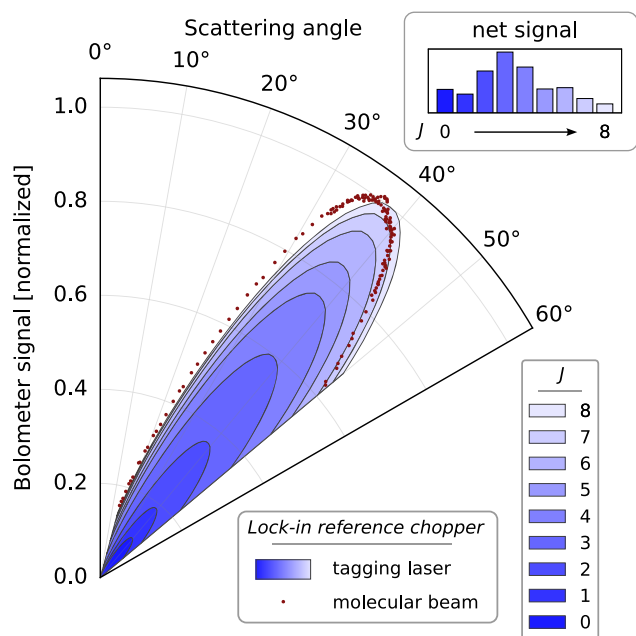
FIG. 9. Comparison of CH_4/Ni(111) scattering distributions measured by summing rovibrational state-resolved data (shaded blue regions) and by a different, state-insensitive technique (red points). Each blue shaded region corresponds to the sum of the sublevel populations for a given rotational level J (ground vibrational state) measured with a continuous molecular beam and the lock-in amplifier synchronized to the tagging laser chopper. The length of the line segment spanning a region at fixed scattering angle is proportional to the measured population for the associated rotational level at that scattering angle. The bar graph in the upper right shows the angle-integrated measured populations for each rotational level. The red points represent the measured bolometer signal with the tagging laser blocked and the lock-in amplifier synchronized to the spinning molecular beam chopper. The tagging data and chopped molecular beam data are separately normalized to yield a peak value of 1.0. The range of measured scattering angles is [15°, 50°]. The incident energy of the incoming molecules is 100 meV, the temperature of the molecular beam nozzle is 300 K, the surface temperature is 473 K, and the angle of incidence is 35°.

frequency of peak response, which typically lies within less than 20 MHz of the frequency obtained after the initial tuning procedure. The detector and tagging laser positions are then scanned synchronously over a series of scattering angles. To separate the contribution to the detector response due to the state-selected molecular flux from the background of scattered laser light, the lock-in amplifier output is recorded twice at each scattering angle, once with the tagging laser tuned on-resonance and another time with the laser tuned 50 MHz off-resonance. From this procedure, we obtain an angular distribution of the scattered flux for a given sublevel. Angular distributions are recorded for all the sublevels of angular momentum J and their contributions summed to obtain a scattering distribution for a given rotational level J.

Shown in red points are measurements made with the tagging laser blocked and the lock-in amplifier synchronized to the rotating molecular beam chopper modulating the incoming flux of molecules. The energy transfer driving the bolometer response in this case is therefore not derived from molecular vibrations stimulated by the tagging laser but rather from the energy of the total internal and external (i.e., translational) motion of the

scattered molecules, along with any heat associated with molecular adsorption on the detector surface. These measurements thus provide, to the extent that the energy per molecule delivered to the bolometer is independent of angle, an independent measure of the angular distribution of total scattering flux against which our tagging measurements can be validated. From inspection, we find satisfactory agreement between the two distributions. The small discrepancies might be explained by the unmeasured contributions from states with $J > 8$ and correlations between scattering angle and molecule–surface energy transfer and/or initial kinetic energy (the spread in incident energies is estimated to be ±15%).

As an aside, we point out that the set of tagging measurements shown in Fig. 9 comprises 34 angular distributions covering all of the rotational sublevels for the three CH_4 nuclear spin isomers (*meta*, *para*, and *ortho*) up through $J = 8$. To allow this quantity of measurements to be completed in a reasonable period of time—one working day in this case—we have found it critical to automate the experimental procedure to the extent we are capable. The most important laborsaving improvements include the following (in descending order of importance):

- coarse and fine control of the tagging laser frequency (Sec. II C 1),
- bolometer rotation and tagging laser mirror translation,
- data recording and continuous logging of sensor data,
- configuration of lock-in amplifier setting, bolometer amplifier gain, and molecular beam chopper rotation and positioning, and
- rotation of polarizing optics.

The last two items form an important part of our procedure for extracting relative state populations from raw bolometer signal via online calibration of bolometer sensitivity and laser excitation fraction. We discuss this procedure in detail in Sec. S1 of the supplementary material. See also Ref. 36 for a repository of the custom software written to control our devices.

III. RESULTS AND DISCUSSION

As a first application of our newly constructed apparatus, we present below a study comparing the rotational state distributions of methane (CH_4) after scattering from a bare and oxidized Ni(111) surface. By exploiting the state- and angle-resolved detection capabilities of the machine, we are able to combine several complementary pieces of evidence that together point toward a dramatic enhancement of molecule–surface energy exchange upon surface oxidation.

The Ni(111) surface, which we refer to as the bare nickel surface, was prepared using a standard recipe of Ar$^+$ sputtering and annealing[40] of a single crystal nickel sample (Surface Preparation Laboratory) followed by a 973 K anneal. The nickel oxide film, which we refer to as the oxidized nickel surface, was prepared by exposing a clean Ni(111) surface held at 300 K to O_2 gas backfilled into the scattering chamber at a pressure of 5×10^{-6} mbar for ~300 s, resulting in a net exposure of ≈1000 L.

Cleanliness and order of the surfaces were verified both before and after experiments by AES and LEED, respectively. We find that the ratio of the peak to peak heights of the 510 eV oxygen KLL and 848 eV nickel LMM Auger spectral features saturates at 1.18

after an exposure of $\approx$100 L. The presence of a NiO(111) oxide film on Ni(111) is readily distinguished from the different chemisorbed O/Ni(111) phases occurring at lower O_2 exposures by a 15% contraction of the fcc(111) hexagonal LEED pattern along with a large increase in LEED spot size.[26] We find that these signatures only appear at O_2 exposures exceeding that required for saturation of the Auger peak ratio. An exposure of 1000 L O_2 gives reproducible Auger spectra and LEED images characteristic of a NiO(111) oxide on Ni(111).[27]

We note that no decrease in the oxygen–nickel Auger peak ratio is observed after several hours of exposure of the oxide surface to the methane molecular beam. Previous studies have used changes in this ratio to estimate rates of methane activation on nickel oxide films,[41] so we take the ratio's constancy over the course of our measurements to indicate a negligible methane reaction (sticking) probability. Similarly, from previous measurements,[42] it is known that methane in the vibrational ground state dissociates on Ni(111) with only negligible probability $\left(<10^{-5}\right)$ at our beam energy and surface temperature.

Our study focuses on vibrationally elastic, rotationally inelastic scattering of methane molecules prepared in their vibrational ground state. For this study, we therefore forgo the pump laser (see Fig. 1), as we did for the measurements presented in Fig. 9 in Sec. II D, and rely instead on the supersonic expansion of the molecular beam for state preparation. The incident molecular beam is formed by collimation of pure CH_4 methane gas escaping from the nozzle and expanding into vacuum. Molecules cool via collisions to their lowest few rotational states during the initial stages of the expansion and at the nozzle temperature used (23 °C) essentially all of the molecules occupy the ground vibrational state. The CH_4 isotopologue of methane has three nuclear spin isomers, viz., p-, o-, and m-CH_4, with total nuclear spins $I = 0, 1, 2$, respectively. m-CH_4 makes up 5/16 of a gas of CH_4 at room temperature[43] and has $J = 0$ and $J = 3$ for its two lowest rotational levels, the $J = 1$ and $J = 2$ states being symmetry forbidden. The relatively large energetic gap between the two states results in a significant ($\approx$90%) concentration of the m-CH_4 population into the $J = 0, M_J = 0$ rovibrational quantum state (ground vibrational state) during supersonic expansion. Furthermore, interconversion among the different nuclear spin isomers in molecule–surface collisions is presumed to occur with only negligible probability; indeed, our own preliminary measurements using a double-resonance pump–probe technique were unable to detect evidence of such interconversion. Scattering m-CH_4 molecules therefore originate from essentially a single incident quantum state so that tagging measurements probing m-CH_4 transitions are truly "state-to-state". For this reason, we present in this study scattering results for the m-CH_4 nuclear spin isomer only. For all scattering measurements described below, the molecules in the incident beam move with a velocity of 1100(70) m s^{-1} and strike the surface at a fixed angle of incidence $\theta_i = 35°$ with respect to the surface normal.

The top panel of Fig. 10 shows rotational distributions for m-CH_4 scattering from the bare and oxidized Ni(111) surface at a surface temperature $T_s = 473$ K obtained with the detector positioned at a scattering angle $\theta_s = 35°$, i.e., the angle of specular reflection. See Sec. S1 of the supplementary material for a description of how relative rotational state populations are extracted from tagging measurements. For some values of J probed, $J = 6, 9,$ and
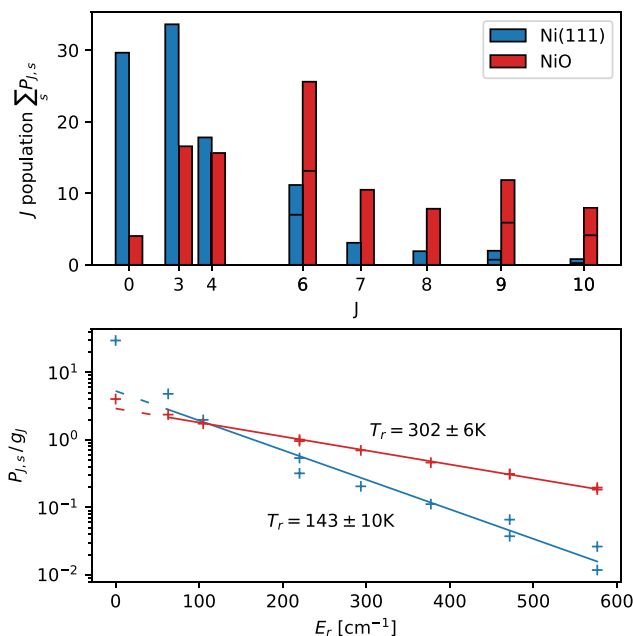
FIG. 10. *Top panel*: rotational state distributions of $J = 0$ m-CH_4 scattering from bare (blue) and oxidized (red) Ni(111) surfaces with $E_t = 100$ meV, $\theta_i = 35°$, $\theta_s = 35°$, and $T_s = 473$ K. $P_{J,s}$ denotes the measured population of the m-CH_4 rotational sublevel with rotational quantum number J and spatial symmetry $s \in \{A1, A2\}$, and $\sum_s$ denotes a sum over the different sublevels of a rotational level J. For J levels with multiple sublevels, the lower and upper bars are of A1 and A2 symmetry, respectively. Populations are plotted as percentage of total measured signal. *Bottom panel*: measured degeneracy-weighted sublevel populations $P_{J,s}/g_J$ (plotted in crosses) vs level energy E_r, with $g_J = 2J + 1$ and $E_r \approx BJ(J + 1)$, where $B = 5.24$ cm^{-1} is the CH_4 rotational constant.[44] Plotted in straight solid lines are accompanying fits to a thermal (Boltzmann) distribution $P_{J,s} \propto e^{-\frac{E_r}{k_B T_r}}$, where k_B is Boltzmann's constant. Color coding retained from upper panel. The contribution from the elastic $J = 0 \to 0$ scattering channel is excluded from the fits.

10, m-CH_4 possesses multiple closely spaced rotational sublevels. So that the figure more clearly represents the distribution of rotational energy, the contributions for these sublevels are summed together, i.e., the bars associated with states of equal J are stacked.

From inspection of the two distributions, it is clear that the degree of rotational excitation measured at the angle of specular scattering is greatly enhanced by oxidation of the nickel surface. To quantify this effect, we compute the effective rotational temperatures T_r of the two distributions, which are obtained by a fit of the populations to a thermal (Boltzmann) distribution and shown in the bottom panel of Fig. 10. Quantifying the degree of rotational excitation by an effective temperature, as opposed to simply computing an population-weighted average of the rotational energy among the states probed, has the benefit of indirectly including estimated contributions for states of higher J not probed. This form of extrapolation is justified by the rather satisfactory quality of the fits, particularly for the oxidized surface data where the unprobed states (i.e., $J > 10$) are expected to be significantly populated. In order to better estimate the contributions from the higher J states, we exclude from the fits the contribution from the elastic $J = 0 \to 0$

channel, which for the bare surface visibly deviates from the best-fit prediction.

From the fits, we find that the T_r derived from the oxidized surface data is more than double that of the bare surface, confirming quantitatively what was qualitatively evident from inspection of the raw distributions. The T_r extracted from the oxidized data lies much closer to the T_s = 473 K temperature of the surface than does the T_r obtained for the bare surface. Lacking any detailed theoretical data to compare our results against, we form from this simple observation the working hypothesis, around which we frame the remaining discussion, that the rotationally cold molecular beam more efficiently equilibrates with the atoms of the oxidized surface than with those of the bare surface. That the relative standard error for T_r reported by the least-squares optimization routine is also higher for the bare surface data ($\frac{\sigma_{T_r}}{T_r}$ = 7%) than the oxidized surface (2%), i.e., that the scattered rotational distribution for the oxidized surface is more "Boltzmann-like," offers a first piece of further evidence for a stronger equilibrating effect of the oxidized surface.

Additional support for the hypothesis can be found from analysis of the relative populations of the sublevels sharing the same J quantum number. Energy eigenstates belonging to different sublevels but of equal J have of course the same total angular momentum but are distinguished, crudely speaking, by the internal axes about which the molecule will prefer to rotate. In thermal equilibrium, these sublevels, which differ in energy by less than 0.03 meV, should be essentially equally populated in the scattered flux. For molecules scattering from the bare surface, however, these sublevels differ significantly in scattering probability. For example, the scattering flux at θ_s = 35° of the J = 6 m-CH$_4$ sublevel of $A1$ symmetry is nearly twice as populated as the J = 6 m-CH$_4$ sublevel of $A2$ symmetry when the molecules scatter from the bare surface. Even larger ratios are found in the bare surface data for the J = 9 and J = 10 energy levels, though their weak overall scattering probabilities leaves open the objection that these disparities originate from scattering from (small) concentrations of surface contaminants or structural defects. In any case, such disparities between sublevel populations are essentially absent in the oxidized surface data, though scattering intensities are strong for all probed sublevels.

Analysis of the state-resolved angular distributions also suggests an enhancement of molecule/surface energy exchange upon surface oxidation. Angular distributions for three different rotational states are displayed in Fig. 11. To permit convenient comparison between bare and oxidized surface data, the plotted scattering intensities for each surface are separately normalized to the total signal averaged over all measured lines and scattering angles and then uniformly scaled to yield a peak scattering intensity of 100 for the J = 0 state scattering from the bare surface. Displayed along with the measurements of the scattering intensity are fits $S(\theta_s; S_o, n, \theta_o)$ of the form

$$S(\theta_s; S_o, n, \theta_o) = S_o \cos^n(\theta_s - \theta_o). \tag{1}$$

The parameters S_o and θ_o characterize respectively the peak amplitude and location, while the exponent n characterizes the sharpness of the peak. From the data, it is clear that while the elastic J = 0 → 0 scattering channel [Fig. 11(a)] for the bare surface is concentrated tightly around specular [n = 41(1), θ_o = 36.8(1)], the corresponding distribution for the oxidized surface is relatively broad [n = 3.3(3)]

and shifted significantly toward surface normal (θ_o = 25.8). The angular distribution of molecules scattering from the bare surface therefore closely resembles that obtained by a simple reflection of the narrowly collimated incident distribution, so that these molecules can be said to retain to a high degree a "memory" of their initial conditions, while the angular distribution of molecules scattering from the oxidized surface appears to possess a weaker memory of their initial conditions and a stronger resemblance to the limiting $\cos\theta_s$ (i.e., n = 1, θ_s = 0°) distribution expected for molecules whose momenta have fully equilibrated with the surface degrees of freedom, i.e., for molecules that were "trapped" by the surface.

Measurements probing molecules excited to the J = 7 rotational state after scattering from the oxidized surface reveal an even stronger broadening and shift toward specular [Fig. 11(b)] than that observed for the J = 0 data. One could rationalize this finding by the simple reasoning that those molecules that couple long enough or strongly enough with the surface to undergo high rotational excitation will also experience greater accommodation of their translational degrees of freedom. The same measurements performed with the bare surface also show an increased broadening compared to J = 0 though with a peak shifted *further* from specular. Indeed, this shift is what one would anticipate for a static and nominally flat Ni(111) surface mediating an intramolecular conversion of translational kinetic energy to rotational kinetic energy. Since a flat surface can only apply forces along the surface normal, it is the molecule's momentum perpendicular to the surface that is necessarily reduced, resulting in super-specular scattering.

Figure 11(c) presents angular distributions of the J = 6 rotational sublevels. Earlier (see Fig. 10 and related discussion) it was observed that, for a fixed detection angle θ_s = 35°, molecules scattering from the bare surface were significantly more likely to scatter into the $A1$ sublevel of the J = 6 rotation level than the $A2$ sublevel, while scattering from the oxidized surface produced scattering of equal intensity for the two sublevels. From inspection of the angular distributions, it is clear that in scattering from the oxidized surface molecules populate essentially equally the two sublevels over the full range of scattering angles measured. Equal population of rotational sublevels is consistent with the scattering flux possessing minimal internal rotational alignment, which is in turn consistent with our picture of the atoms of the oxidized surface serving as a thermal bath acting to suppress anisotropy in the internal orientation of molecular rotation. Scattering from the bare surface however produces peaks for the two sublevels that differ considerably in terms of not only their peak amplitude [$S_{o,A1}/S_{o,A2}$ = 1.75(1)] but also their sharpness [n_{A1}/n_{A2} = 1.35(5)] and peak location [$\theta_{o,A1} - \theta_{o,A2}$ = 5.2(2)°]. This lack of thermalization of the rotational sublevels in scattering from the Ni(111) surface is in line with our hypothesis of the CH$_4$/Ni(111) collision being largely impulsive.

One at this point might reasonably ask what more detailed properties of the CH$_4$/Ni(111) interaction potential might be learned from these disparities in the peak properties of the sublevel-resolved angular distributions. Among the necessary first steps of such an investigation would of course be to identify in what respects do the J = 6 $A1$ and $A2$ states differ. Though we reserve detailed discussion of the topic of rotational alignment in the CH$_4$-surface scattering for a future publication, we include for completeness in Sec. S3 (Fig. S4) of the supplementary material plots of the "angular momentum probability surfaces"[45] for the two states. These plots show that
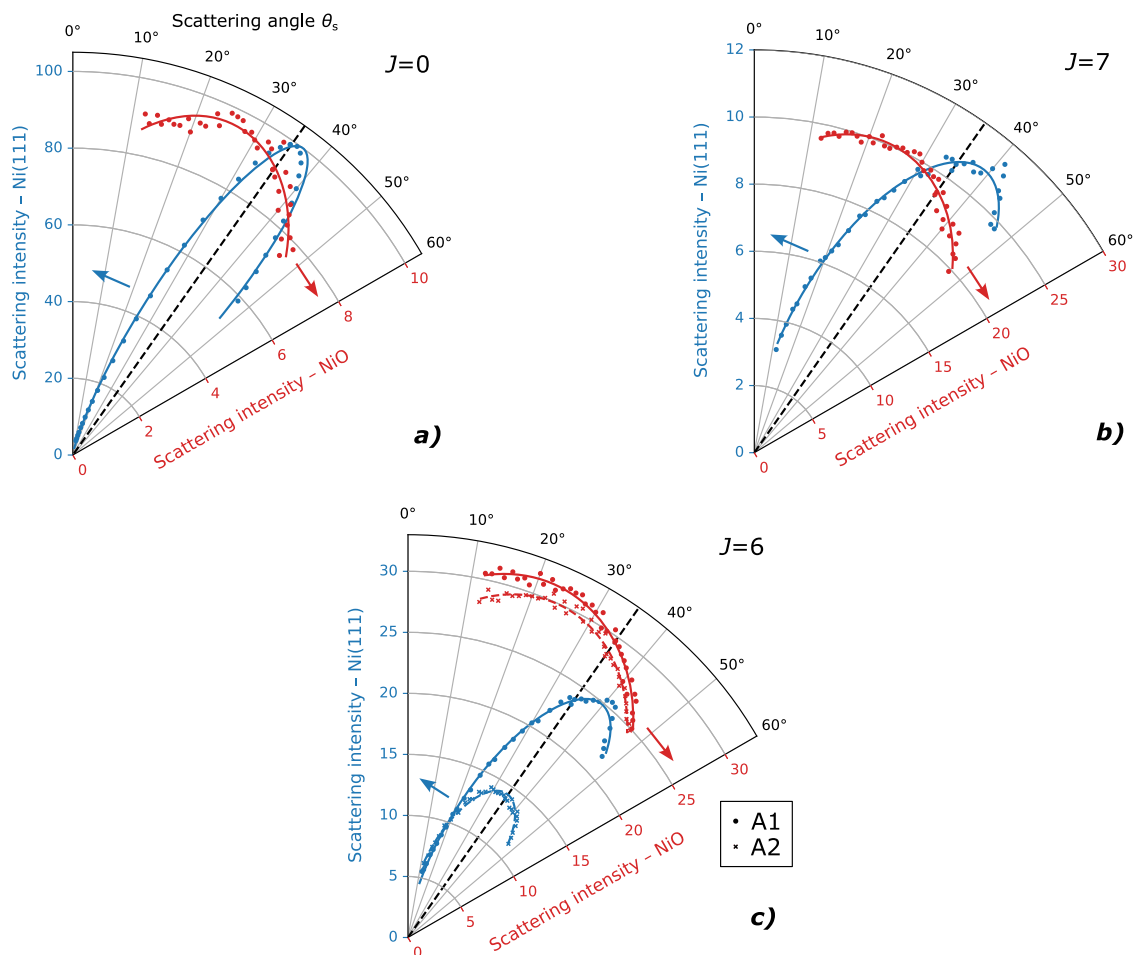
FIG. 11. State-resolved angular distributions for m-CH$_4$ scattering from Ni(111) (blue points) and NiO/Ni (red points) at T_s = 473 K. E_t = 100 meV, θ_i = 35°. The rotational states probed are $J = 0, 7, 6$ for subfigures (a)–(c) respectively. The $A1$ ($A2$) $J = 6$ sublevel is marked by points (crosses). Solid lines show fit to Eq. (1) and the black dashed line indicates the specular angle. Scattering intensity normalization convention explained in text.

the $A1$ state is characterized by a preference for rotation about the C–H bond axes and an aversion to rotation about the axes bisecting the bonds, while the $A2$ state is best characterized by an aversion to rotation about the axes perpendicular to planes formed by two bonds.

Figure 12 shows the best-fit n, θ_o, and S_o values for all the probed m-CH$_4$ J levels. All fits are of a quality comparable to those shown in Fig. 11. Along with the bare and oxidized surface data for the T_s = 473 K surface temperature that we have up to now been discussing (i.e., Figs. 10 and 11), we include for completeness results from measurements taken with the bare surface at T_s = 873 K and results with the oxidized surface at T_s = 300 K. In the following discussion of Fig. 12, we restrict our attention to the T_s = 473 K data. See Fig. 13 and associated text for discussion of surface temperature effects.

The trends revealed by Fig. 12 lend further support to the hypothesis of surface oxidation leading to a more efficient equilibration of molecular rotation and translation during scattering. To

elaborate, we first note that across all J values we find for the oxidized surface data a lower exponent n and a peak location θ_o skewed closer to surface normal, both indicative of an evolution toward the limiting $\cos \theta_s$ distribution. The enhanced S_o at higher J shows that the evidence for greater rotational heating demonstrated in Fig. 10 for a fixed observation angle holds when the full range of accessible scattering angles is taken into account.

During our earlier discussion of the $J = 0$ and $J = 7$ angular distributions plotted in Fig. 11, we identified two correlations—both of which we argued to be consistent with our working hypothesis—associated with increasing rotational quantum number J: an increase in peak broadening and skewing toward normal for the oxidized surface and a skewing away from normal for the bare surface. Inspection of Fig. 12 shows that both trends are found to hold upon examination of the full spectrum of probed J levels.
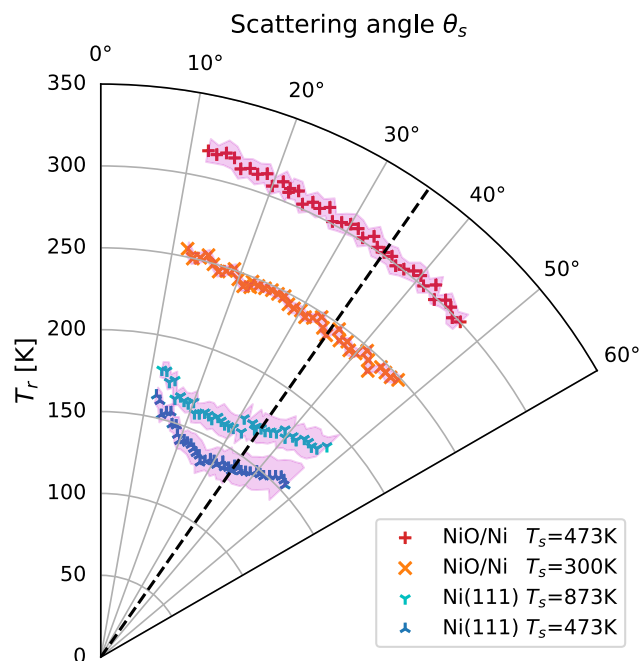
To investigate further the hypothesis of oxidation leading to a more efficient equilibration of a scattering methane beam, we
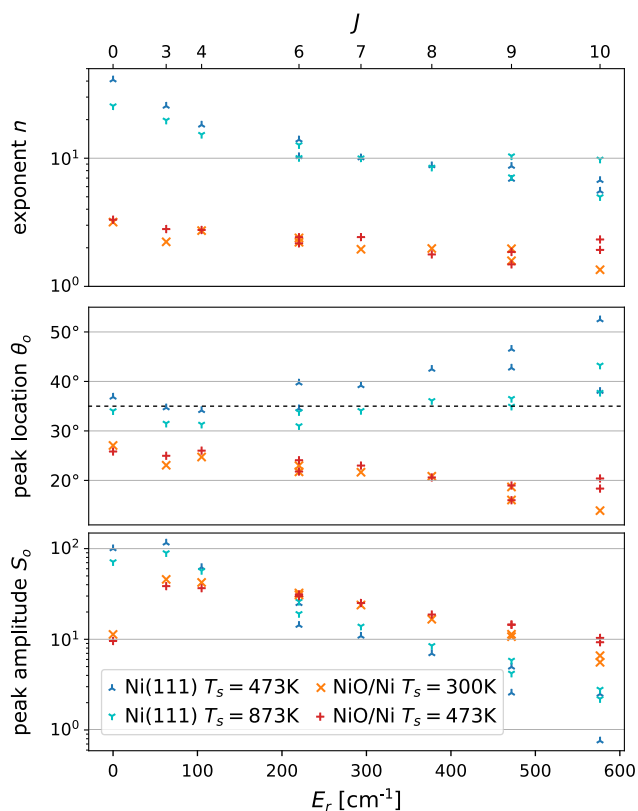
FIG. 12. Plots of the parameter values extracted from fits of the state-resolved angular distributions to Eq. (1). Dashed line in the middle panel indicates the spec-ular angle $\theta_s = 35°$. Scattering amplitude normalization is the same as in Fig. 11. The angular distribution of $J = 10$ A2 transition for the NiO surface at $T_s = 300$ K was measured to be flat within experimental error and so its best-fit θ_o and n parameter values are omitted from the plot.

FIG. 13. Angular distribution of effective rotational temperature T_r defined in Fig. 10. $E_t = 100$ meV, $\theta_i = 35°$. Shaded areas surrounding markers denote 68% confidence intervals derived from standard errors reported by fitting routine. Black dashed line marks the specular angle.

vary the surface temperatures of the bare and oxidized surfaces and compare the changes in the effective rotational temperatures T_r. Due to practical considerations related to maintaining clean and well-ordered surfaces for the several hours required to complete an experiment, the surface temperature changes were restricted to an increase to 873 K and a decrease to 300 K for the bare and oxidized surface, respectively.

Figure 13 shows angle-resolved plots of the effective rotational temperatures T_r for the four experimental conditions studied. Rota-tional temperatures are determined in the same way as was done for Fig. 10. Consistent with the previous evidence presented casting the bare nickel surface as a static participant in the scattering event, we find the surface temperature of the bare surface exerts only a weak influence on the scattered rotational temperature, with a large (84%) increase in the bare nickel surface temperature producing only a small ($\approx 13\%$) increase in the computed T_r. A small 37% decrease in the oxidized surface temperature however leads to a relatively large ($\approx 22\%$) drop in T_r, in line with what one would expect for a scatter-ing event characterized by a "heating" of molecular rotation by the surface. To quantify the efficacy of the response in T_r to changes in T_s, we can look at the ratio $\frac{\Delta T_r/T_r}{\Delta T_s/T_s}$, from which we can conclude that

the oxide surface is $\frac{22}{37}/\frac{13}{84} \approx 3.8$ times more effective than the bare surface in heating the molecules' rotational motion.

Finally, we identify for the bare surface data, as compared to that of the oxidized surface, relatively large standard errors associated with the best-fit estimates of T_r, particularly at large scattering angles. For many fitting procedures, including the Levenberg–Marquardt least-squares algorithm[46,47] employed in our fits, a large standard error is consistent with a poor goodness-of-fit, suggesting that the m-CH$_4$ rotational state distributions obtained from scattering from the bare surface conform relatively poorly to a thermal distribution.

To further explore this suggestion, we analyze for the $T_s = 473$ K bare and oxidized datasets the fit residuals obtained by taking for each measured scattering angle and probed substate the difference between the measured substate population and its best-fit predicted value at that scattering angle. See the lower panel of Fig. 10 for an example of a fit performed at a scattering angle of $\theta_s = 35°$. The residuals are plotted in Fig. 14. To permit meaningful comparison across sublevels, scattering angle, and surface compo-sition, the residuals here are plotted as percent deviations of the measured value from its best-fit predicted value. Note also that, in order to best assess the degree to which the measured distribu-tions match a thermal distribution, the residuals here are computed from fits which, unlike those underlying Figs. 10 and 13, include the contribution from the elastic $J = 0 \rightarrow 0$ scattering channel.

From inspection of the plots, it is clear that the residuals computed from bare surface data, compared to those computed from the oxidized surface data, show significantly more pronounced
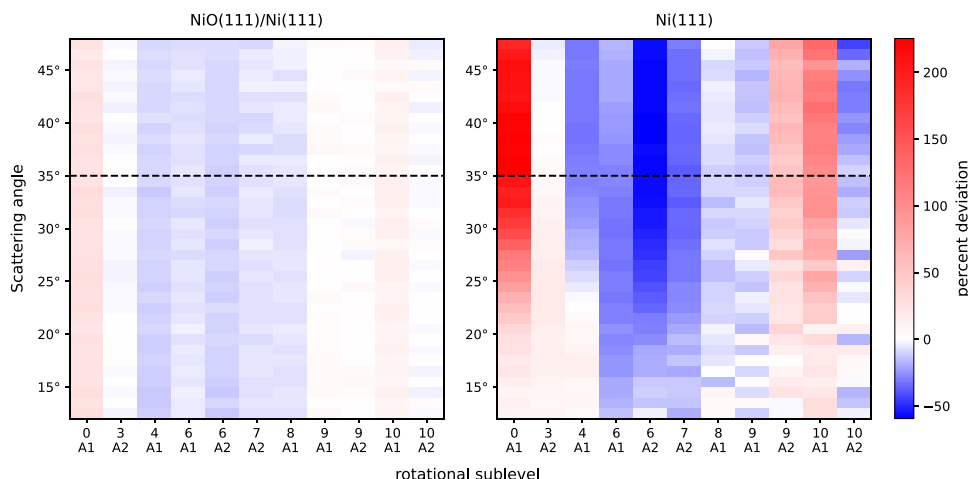
FIG. 14. Plot of residuals to fits of measured rotational distribution to a thermal (Boltzmann) distribution for all measured scattering angles for the bare (right) and oxidized (left) surface datasets measured with the surface temperature held at 473 K. Residuals are plotted as percent deviation of measured degeneracy-weighted population $P_{J,s}/g_J$ from best-fit prediction. The dashed lines mark the angle of specular scattering. The fits from which the residuals are computed include the contribution from the elastic $J = 0 \rightarrow 0$ scattering channel.

and detailed structure. In addition, the residual amplitudes for the bare surface data visibly intensify with increasing scattering angle, while for the oxidized surface data the residuals show little variation with scattering angle. While lacking the computational capabilities to permit a full accounting of the precise form of the measured rotational distributions, we argue that the observed trend in scattering angle and goodness-of-fit observed for the bare surface data is in any case consistent with our hypothesis of weak $CH_4 \leftrightarrow Ni(111)$ energetic coupling. As pointed out earlier, elastic scattering of an initially nonrotating molecule from a flat surface is necessarily super-specular. Therefore, to the extent that the Ni(111) surface is flat and stiff, one would expect a significant fraction of the super-specular flux to originate from quasi-elastically scattered molecules whose rotational distribution is determined by the particular details of the molecule–surface interaction potential and thus unlikely to be described accurately by a thermal distribution. The comparatively weak amplitude of the residuals computed for the oxidized surface data, along with their lack of variation with scattering angle, is likewise consistent with our hypothesis of facile $CH_4 \leftrightarrow NiO(111)/Ni(111)$ energy exchange where a collision trajectory proceeds through multiple "soft bounces." For such trajectories, one expects detailed structure in the rotational populations as well as strong angular correlations, to be largely suppressed by coupling of molecule's rotation and translation to the surface degrees of freedom.

In closing the discussion, we mention that a number of the observed changes in scattering behavior upon surface oxidation can alternatively be explained by a stronger lateral surface corrugation for the oxidized surface as indicated by helium scattering measurements (see end of Sec. I). Certainly, broad angular distributions are an expected consequence of corrugated surfaces, and to a certain extent one also anticipates greater rotational excitation, though in this case one must also consider the complicating factor of corrugation in the molecule's rotational coordinates.

Surface corrugation alone however fails to adequately account for many of the other qualitative changes observed in the methane scattering behavior. Static corrugation for example cannot explain the strong temperature dependence on the effective rotational temperature, nor can it explain the identical angular distributions of the

degenerate rotational sublevels or the strong conformance of the rotational distribution to a thermal (Boltzmann) distribution. So, while we cannot exclude surface corrugation as a partial explanation of the observed effects of surface oxidation on methane scattering, we find the hypothesis of an enhancement in molecule–surface energetic coupling to be at once a more comprehensive and economical explanation.

IV. CONCLUSION

To summarize, we describe a novel UHV molecule/surface scattering apparatus with the capabilities of quantum state preparation and quantum state resolution accomplished using a pair of CW mid-IR OPO lasers in combination with bolometric detection. The state preparation and detection techniques are applicable to any molecule with an infrared-active vibrational transition. Furthermore, the surface and detector are both rotatable, permitting independent variation of the incident and detection/scattering angles. We present as a first application of the instrument scattering measurements comparing rotational inelasticity in $J = 0$ m-CH_4 scattering from a Ni(111) surface and a NiO(111)/Ni(111) oxide film.

Oxidation of the nickel surface is found to dramatically alter the methane scattering behavior in several regards. First, molecules scattering from the oxidized surface are significantly more excited rotationally than those scattering from the bare surface. The degree of rotational excitation mediated by the oxidized surface is characterized by an effective rotational temperature more than twice that measured from the bare surface at the same surface temperature. Second, molecules scatter from the oxidized surface into a broad distribution with a peak angle trending toward surface normal with increasing rotational quantum number J, while scattering from the bare surface produces a narrow distribution with a peak angle trending away from normal with higher J. Furthermore, nearly degenerate rotational substates of equal J populate the bare surface scattered flux with markedly different angular distributions in terms of both shape and intensity, while for the oxidized surface these substates yield essentially indistinguishable angular distributions. In addition, the effective rotational temperature of molecules

scattering from the oxidized surface is found to be almost four times more sensitive to changes in surface temperature than that of the bare surface. Finally, the distribution of rotational state populations produced by scattering from bare surface shows much larger deviations from their best-fit thermal distributions, particularly at wide scattering angles, than do those produced by scattering from the oxidized surface.

We attribute these differences in scattering behavior to an oxidation-induced enhancement in CH_4-surface energy exchange during collisions. We hope the unprecedented level of microscopic insight offered by the state-to-state measurements presented here will inspire theoretical investigation into the nature of molecule–surface energy transfer in these two systems.

SUPPLEMENTARY MATERIAL

See the supplementary material document for detailed discussion of scattered state population estimation, presentation of helium atom scattering measurements from surfaces studied, and discussion of internal alignment of molecular rotation.

AUTHOR DECLARATIONS

Conflict of Interest

The authors have no conflicts to disclose.

Author Contributions

R.D.B. conceptualized the project, secured funding, and supervised the project. D.J.A. designed the described apparatus with support from B.-J.C. and R.D.B., B.-J.C. managed construction and executed testing of the apparatus. P.F. and C.S.R. improved the experimental setup, including the conceptualization and implementation of the reported automation. P.F. and C.S.R. designed the experiment. P.F. performed the measurements with support from C.S.R., P.F. and C.S.R. analyzed the data. C.S.R. wrote the manuscript with support from P.F., R.D.B., D.J.A., and B.-J.C.

Christopher Scott Reilly: Conceptualization (equal); Data curation (equal); Formal analysis (equal); Investigation (equal); Methodology (equal); Project administration (equal); Software (equal); Validation (equal); Visualization (equal); Writing – original draft (equal); Writing – review & editing (equal). **Patrick Floβ**: Conceptualization (lead); Data curation (equal); Formal analysis (equal); Investigation (equal); Methodology (equal); Project administration (equal); Software (equal); Validation (equal); Visualization (equal); Writing – original draft (supporting); Writing – review & editing (supporting). **Bo-Jung Chen**: Conceptualization (supporting); Methodology (equal); Writing – original draft (supporting). **Daniel J. Auerbach**: Conceptualization (supporting); Investigation (supporting); Methodology (equal); Project administration (equal); Supervision (lead); Writing – original draft (supporting); Writing – review & editing (supporting). **Rainer D. Beck**: Conceptualization (equal); Funding acquisition (equal); Methodology (equal); Project administration (equal); Resources (equal); Supervision (equal); Writing – original draft (equal); Writing – review & editing (equal).

DATA AVAILABILITY

The data that support the findings of this study are available from the corresponding author upon reasonable request.

REFERENCES

[1] J. H. Larsen and I. Chorkendorff, "From fundamental studies of reactivity on single crystals to the design of catalysts," Surf. Sci. Rep. **35**, 163–222 (1999).

[2] C. H. Christensen and J. K. Nørskov, "A molecular view of heterogeneous catalysis," J. Chem. Phys. **128**, 182503 (2008).

[3] F. Frenkel, J. Häger, W. Krieger, H. Walther, C. T. Campbell, G. Ertl, H. Kuipers, and J. Segner, "Rotationally inelastic gas-surface scattering investigated by laser-induced fluorescence," Phys. Rev. Lett. **46**, 152–155 (1981).

[4] M. Asscher, W. L. Guthrie, T.-H. Lin, and G. A. Somorjai, "Vibrational and rotational energy distribution of NO scattered from the Pt(111) crystal surface: Detection by two-photon ionization," Phys. Rev. Lett. **49**, 76–79 (1982).

[5] T. E. Gough, R. E. Miller, and G. Scoles, "Infrared laser spectroscopy of molecular beams," Appl. Phys. Lett. **30**, 338–340 (1977).

[6] T. W. Francisco, N. Camillone III, and R. E. Miller, "Rotationally inelastic scattering of C_2H_2 from LiF(100): Translational energy dependence," Phys. Rev. Lett. **77**, 1402–1405 (1996).

[7] A. C. Wight, M. Penno, and R. E. Miller, "Sequential vibrational relaxation of polyatomic molecules at surfaces: C_2HD and C_2H_2 scattered from LiF(001)," J. Chem. Phys. **111**, 8622–8627 (1999).

[8] A. C. Wight and R. E. Miller, "Vibrational quenching of acetylene scattered from LiF(001): Trapping desorption versus direct scattering," J. Chem. Phys. **109**, 8626–8634 (1998).

[9] A. C. Wight and R. E. Miller, "Rainbow scattering of methane from LiF(100): Probing the corrugation and anisotropy of the gas-surface potential," J. Chem. Phys. **109**, 1976–1982 (1998).

[10] A. Henderson and R. Stafford, "Low threshold, singly-resonant CW OPO pumped by an all-fiber pump source," Opt. Express **14**, 767–772 (2006).

[11] D. B. Foote, M. J. Cich, W. C. Hurlbut, U. Eismann, A. T. Heiniger, and C. Haimberger, "High-resolution, broadly-tunable mid-IR spectroscopy using a continuous wave optical parametric oscillator," Opt. Express **29**, 5295–5303 (2021).

[12] J. Werdecker, M. E. van Reijzen, B.-J. Chen, and R. D. Beck, "Vibrational energy redistribution in a gas-surface encounter: State-to-state scattering of CH_4 from Ni(111)," Phys. Rev. Lett. **120**, 053402 (2018).

[13] J. Werdecker, B. J. Chen, M. E. Van Reijzen, A. Farjamnia, B. Jackson, and R. D. Beck, "State-to-state methane-surface scattering as a probe of catalytic activity," Phys. Rev. Res. **2**, 043251 (2020).

[14] R. D. Beck, P. Maroni, D. C. Papageorgopoulos, T. T. Dang, M. P. Schmid, and T. R. Rizzo, "Vibrational mode-specific reaction of methane on a nickel surface," Science **302**, 98–100 (2003).

[15] D. R. Killelea, V. L. Campbell, N. S. Shuman, and A. L. Utz, "Bond-selective control of a heterogeneously catalyzed reaction," Science **319**, 790–793 (2008).

[16] D. R. Killelea, V. L. Campbell, N. S. Shuman, R. R. Smith, and A. L. Utz, "Surface temperature dependence of methane activation on Ni(111)," J. Phys. Chem. C **113**, 20618–20622 (2009).

[17] B. L. Yoder, R. Bisson, and R. D. Beck, "Steric effects in the chemisorption of vibrationally excited methane on Ni(100)," Science **329**, 553–556 (2010).

[18] B. L. Yoder, R. Bisson, P. M. Hundt, and R. D. Beck, "Alignment dependent chemisorption of vibrationally excited CH_4 (v_3) on Ni(100), Ni(110), and Ni(111)," J. Chem. Phys. **135**, 224703 (2011).

[19] L. Chen, H. Ueta, R. Bisson, and R. D. Beck, "Vibrationally bond-selected chemisorption of methane isotopologues on Pt(111) studied by reflection absorption infrared spectroscopy," Faraday Discuss. **157**, 285–295 (2012).

[20] N. Chen, Y. Huang, and A. L. Utz, "State-resolved reactivity of methane ($v_2 + v_4$) on Ni(111)," J. Phys. Chem. A **117**, 6250–6255 (2013).

[21] A. Al Taleb and D. Farías, "Coherent quantum scattering of CH_4 from Ni(111)," Phys. Chem. Chem. Phys. **19**, 21267–21271 (2017).

[22] P. H. Holloway and J. B. Hudson, "Kinetics of the reaction of oxygen with clean nickel single crystal surfaces: II. Ni(111) surface," Surf. Sci. **43**, 141–149 (1974).

[23] H. Conrad, G. Ertl, J. Küppers, and E. E. Latta, "A LEED/UPS study on the interaction of oxygen with a Ni(111) surface," Solid State Commun. **17**, 497–500 (1975).

[24] G. T. Tyuliev and K. L. Kostov, "XPS/HREELS study of NiO films grown on Ni(111)," Phys. Rev. B **60**, 2900–2907 (1999).

[25] T. Okazawa, T. Nishizawa, T. Nishimura, and Y. Kido, "Oxidation kinetics for Ni(111) and the structure of the oxide layers," Phys. Rev. B **75**, 033413 (2007).

[26] J. I. Flege, A. Meyer, J. Falta, and E. E. Krasovskii, "Self-limited oxide formation in Ni(111) oxidation," Phys. Rev. B **84**, 115441 (2011).

[27] H. Kuhlenbeck, S. Shaikhutdinov, and H.-J. Freund, "Well-ordered transition metal oxide layers in model catalysis—A series of case studies," Chem. Rev. **113**, 3986–4034 (2013).

[28] P. Cantini, R. Tatarek, and G. P. Felcher, "Diffraction of a beam of monoenergetic helium atoms from the (001) face of nickel oxide," Phys. Rev. B **19**, 1161–1171 (1979).

[29] A. al Taleb, G. Anemone, D. Farías, and R. Miranda, "Acoustic surface phonons of graphene on Ni(111)," Carbon **99**, 416–422 (2016).

[30] A. Tamtögl, E. Bahn, J. Zhu, P. Fouquet, J. Ellis, and W. Allison, "Graphene on Ni(111): Electronic corrugation and dynamics from helium atom scattering," J. Phys. Chem. C **119**, 25983–25990 (2015).

[31] Surface corrugations as measured by one atom/molecule do not however transfer straightforwardly to other molecules. For example, al Taleb et al.[21] extract a surface corrugation in CH4/Ni(111) scattering of 0.02-0.10 Å, measurably stronger than that measured for helium scattering. al Taleb et al. go on to explain that molecule scattering from LiF(100) however shows the opposite trend, with surface corrugation depths of 0.3 and 0.1 Å as measured by helium and methane, respectively.

[32] H. Chadwick, P. M. Hundt, M. E. van Reijzen, B. L. Yoder, and R. D. Beck, "Quantum state specific reactant preparation in a molecular beam by rapid adiabatic passage," J. Chem. Phys. **140**, 034321 (2014).

[33] D. A. King and M. G. Wells, "Molecular beam investigation of adsorption kinetics on bulk metal targets: Nitrogen on tungsten," Surf. Sci. **29**, 454–482 (1972).

[34] D. J. Auerbach, C. A. Becker, J. P. Cowin, and L. Wharton, "UHV application of spring-loaded teflon seals," Rev. Sci. Instrum. **49**, 1518–1519 (1978).

[35] K. Bergmann, W. Demtröder, and P. Hering, "Laser diagnostic in molecular beams," Appl. Phys. **8**, 65–70 (1975).

[36] C. Reilly and P. Floß (2023). "Beck lab experimental control software," Github. https://github.com/creilly/becksoftware.

[37] B. G. Lindsay, K. A. Smith, and F. B. Dunning, "Control of long-term output frequency drift in commercial dye lasers," Rev. Sci. Instrum. **62**, 1656–1657 (1991).

[38] B. L. Yoder, "Experimental setup," in Steric Effects in the Chemisorption of Vibrationally Excited Methane on Nickel (Springer, 2012), pp. 19–49.

[39] R. C. Hilborn, "Einstein coefficients, cross sections, f values, dipole moments, and all that," Am. J. Phys. **50**, 982–986 (1982).

[40] R. G. Musket, W. McLean, C. A. Colmenares, D. M. Makowiecki, and W. J. Siekhaus, "Preparation of atomically clean surfaces of selected elements: A review," Appl. Surf. Sci. **10**, 143–207 (1982).

[41] R. A. Campbell, J. Szanyi, P. Lenz, and D. Wayne Goodman, "Methane activation on clean and oxidized Ni(100)," Catal. Lett. **17**, 39–46 (1993).

[42] R. Bisson, M. Sacchi, T. T. Dang, B. Yoder, P. Maroni, and R. D. Beck, "State-resolved reactivity of $CH_4(2v_3)$ on Pt(111) and Ni(111): Effects of Barrier height and transition state location," J. Phys. Chem. A **111**, 12679–12683 (2007).

[43] E. B. Wilson, "The statistical weights of the rotational levels of polyatomic molecules, including methane, ammonia, benzene, cyclopropane and ethylene," J. Chem. Phys. **3**, 276–285 (1935).

[44] D. L. Gray and A. G. Robiette, "Simultaneous analysis of the v_2 and v_4 bands of methane," Mol. Phys. **32**, 1609–1625 (1976).

[45] S. M. Rochester and D. Budker, "Atomic polarization visualized," Am. J. Phys. **69**, 450–454 (2001).

[46] D. W. Marquardt, "An algorithm for least-squares estimation of nonlinear parameters," J. Soc. Ind. Appl. Math. **11**, 431–441 (1963).

[47] K. Levenberg, "A method for the solution of certain non-linear problems in least squares," Q. Appl. Math. **2**, 164–168 (1944).